How contact stiffness and density determine stress-dependent elastic moduli: a micromechanics approach

Choong-Ki Chung · Eui-Ryong Jang ·
Sung-Ha Baek · Young-Hoon Jung

Abstract To investigate the origin of the stress-level dependency of soil elasticity, a series of stress-path experiments were simulated for loose and dense soil specimens with three different contact surfaces. In the discrete element analyses, an assumption was introduced in which the contact body had the geometry of an elastic sphere with local, axi-symmetric irregularity. To evaluate the cross-anisotropic elastic shear moduli, small-strain cyclic shear tests were simulated under stress conditions along four stress-probing paths. For dense specimens with high coordination numbers, the internal structure was represented by the degree of fabric anisotropy and the coordination number remained unchanged during shearing, thus leading to the coincidence of the sum of the exponents in the contact stiffness model. For the loose specimens with low coordination numbers, the fabric structure evolved continuously during shearing, which resulted in the increase of the exponents in the power function of the elastic modulus. The rearrangement of particles and the transition of contact-force chains, along with the evolution of the fabric, manifested as increasing dependency of the elastic moduli on the stresses in such loose specimens.

C.-K. Chung · S.-H. Baek
Department of Civil and Environmental Engineering,
Seoul National University, Kwanak-gu, Seoul 151-744,
Republic of Korea

E.-R. Jang
Civil and Environmental Engineering and Design Group,
Hyungdai Engineering and Construction Co., Ltd,
Seoul 110-920, Republic of Korea

Y.-H. Jung (✉)
Department of Civil Engineering, College of Engineering,
Kyung Hee University, 1732 Deogyeong-daero, Giheung-Gu,
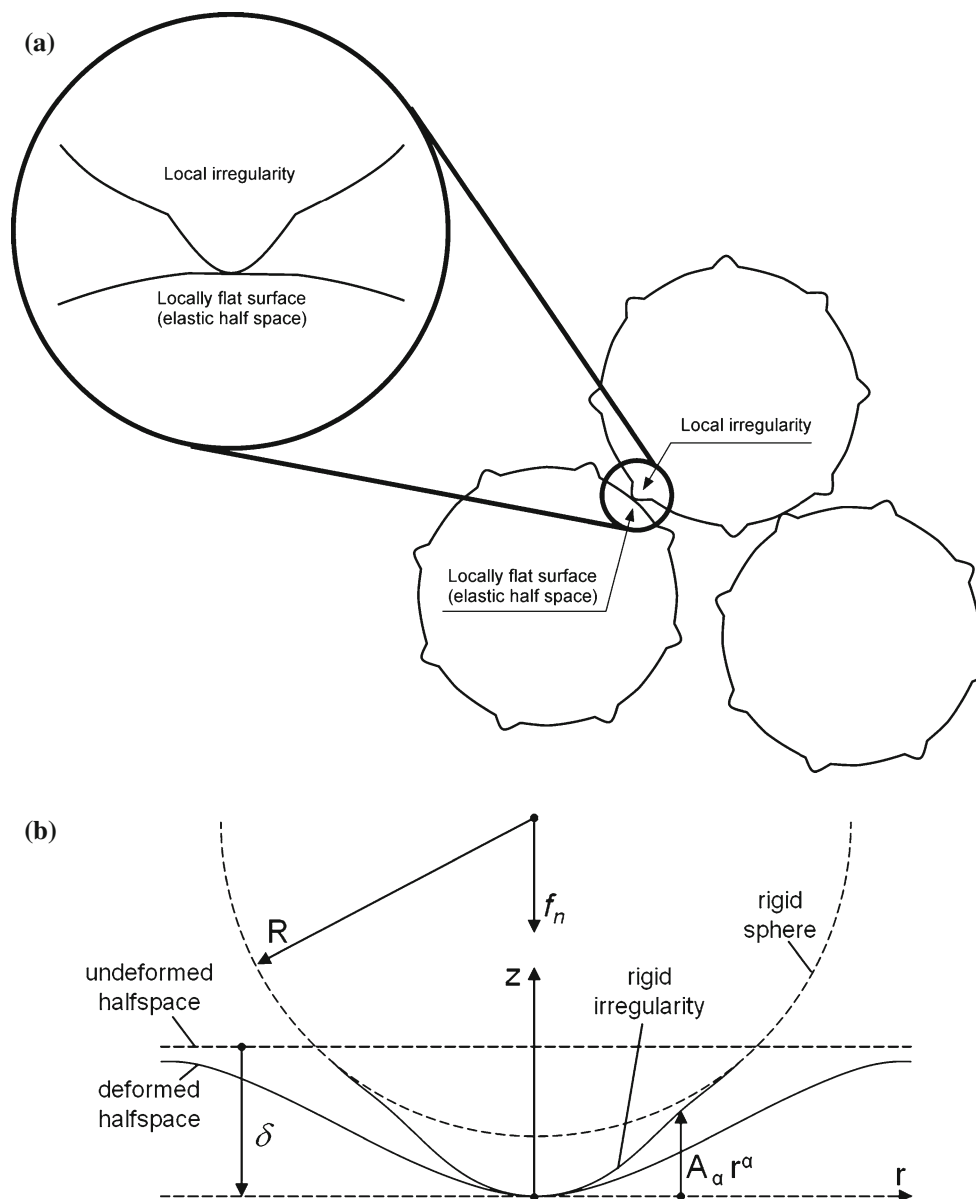Yongin-Si, Gyeonggi-Do 446-401, Republic of Korea
e-mail: jyounghoon@khu.ac.kr

1 Introduction

Stress-level-dependent elasticity is a major feature of soil behavior that needs to be investigated independently within the framework of micromechanics theory. The nonlinear anisotropic elastic response, which has commonly been observed in a large amount of experimental data, can be represented by a well-known empirical equation of three-dimensional elastic moduli [1] given by the following equation:

$$G_{ij} = C_{ij} p_a f(e)(\sigma_i'/p_a)^m (\sigma_j'/p_a)^n \tag{1}$$

where G_{ij} is the elastic shear modulus in the i–j plane, C_{ij} is a dimensionless constant relating to the directional properties of the elastic shear moduli, p_a is the atmospheric pressure, used as a normalizing constant, $f(e)$ is the void ratio function, σ_i' and σ_j' are the principal stresses in the i and j directions respectively, and the exponents m and n are material constants. The sum of exponents m and n (hereafter referred to as s) determines the magnitude of the stress-level dependency of the elastic stiffness of soils. While the stress-level dependency of soil elasticity has long been known, the physical origin of this relationship has not yet been clarified.

The particular form of the power function in Eq. (1) has drawn researchers to investigate an explicit relationship between the elastic response of soils and theoretical contact equations. For instance, Hardin and Blandford [1] explained that in Eq. (1), s is analog to the power of 1/3 in the classical solution of the elastic moduli for a regular assembly of elastic spheres [2]. Cascante and Santamarina [3] argued

Fig. 1 Geometry of contact surface. **a** Contacting particles with local irregularities, **b** geometry of contact surface (after Jäger [12])

that under conditions of isotropic stress, s is determined by the contact-force–displacement relationship, regardless of what mechanisms caused the contact deformation. Jung and Chung [4] investigated the stress-level dependency of cross-anisotropic elastic moduli in granular soils via the analytical micromechanics theory. They showed that under conditions of isotropic stress, the power function of normal contact stiffness manifests itself in the sum of exponents, s, whereas under conditions of anisotropic stress, the evolution of the fabric also has a significant influence on s in the power function.

In experiments, a recent survey of data from resonant column testing [5] for both sands and clays showed that s has

been found to vary between approximately 0.4 and 0.6, with a value of 0.5 having been observed by many researchers. By comparing wave velocities, Lee and Huang [6] showed that s becomes larger as the grains of sand became more angular. Kohata et al. [7] reported that s was nearly 0.5 for various sands with minor angles on their contact surfaces, zero for soft mudstone and tuff featuring flat contact surfaces, and 0.8 for weathered granite, which likely had an angular contact surface.

Clayton [8] recently proposed three factors that might influence the shear modulus of a granular material at very small strain levels: the void ratio, inter-particle contact stiffness, and deformation and flexing within individual
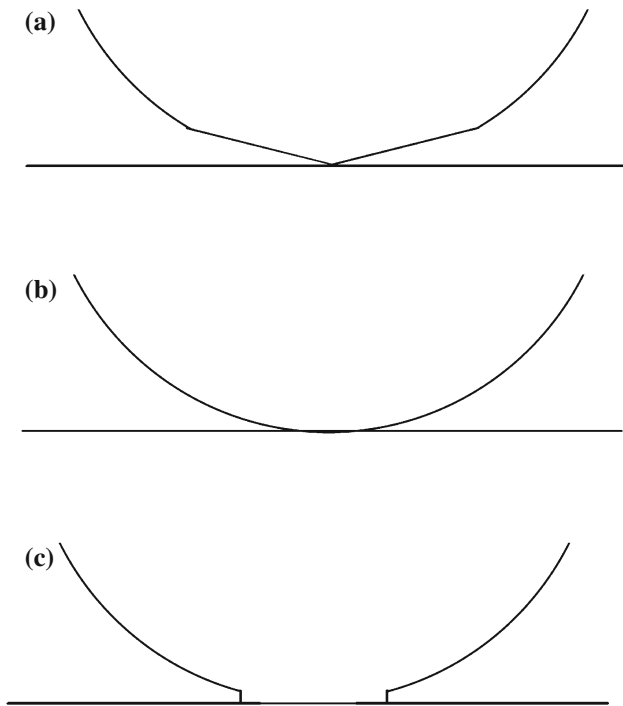
(a)

(b)

(c)

Fig. 2 Three types of contact geometry. **a** Conical contact surface, **b** spherical contact surface, **c** flat contact surface

Table 1 Model parameters used in the DEM simulations

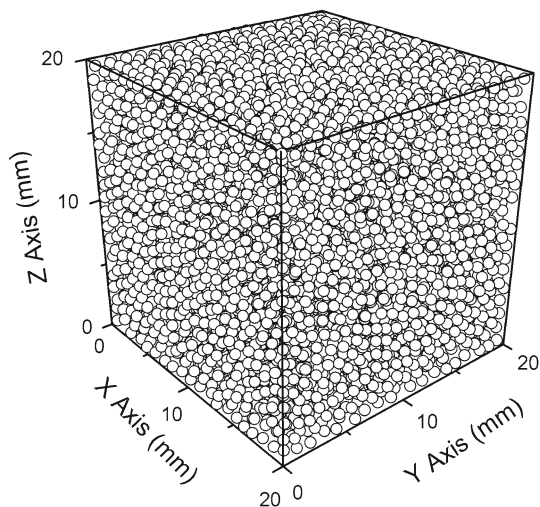| Number of particles	10,000
Radius of particle	0.5 mm
Initial specimen size	20 mm × 20 mm × 20 mm
Inter-particle friction angle	26.5°
Elastic properties of particles	Elastic shear modulus: 30 GPa
	Poisson's ratio: 0.15
Boundary conditions	Rigid boundary condition (Rigid Wall)

Fig. 3 Assembly of particles after preparation

Table 2 Configuration of the initial specimens after isotropic compression

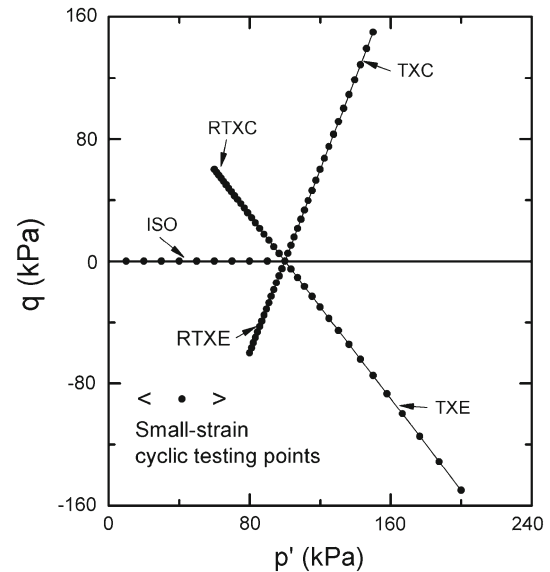| Contact geometry	Density	Initial C_n	Initial void ratio
Conical contact	Dense	5.90	0.555
$\alpha = 1$	Loose	3.91	0.567
Spherical contact	Dense	5.73	0.558
$\alpha = 1$	Loose	3.50	0.572
Flat contact	Dense	5.62	0.559
$\alpha = \infty$	Loose	3.53	0.572

Fig. 4 Applied stress paths and the stress points for cyclic loadings

Table 3 Triaxial experiments performed for stress probe tests

Test	Description
RTXE	Reduced triaxial extension test, decreasing axial stress with constant radial stress
TXC	Triaxial compression test, increasing axial stress with constant radial stress
RTXC	Reduced triaxial compression test, decreasing radial stress with constant axial stress
TXE	Triaxial extension test, increasing radial stress with constant axial stress

particles. When considering minor changes in the void ratio and limited particle deformation under service loading in granular soils, it is obvious that the shear modulus the value of s is mostly affected by the inter-particle contact stiffness, which itself depends on particle mineralogy, angularity and roughness.
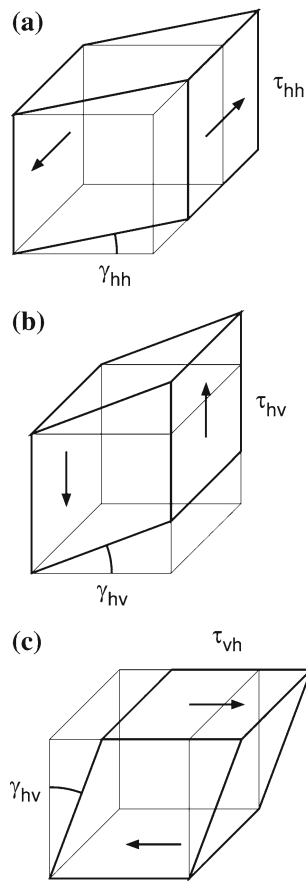
(a)

(b)

(c)

Fig. 5 Three different shearing modes for small cyclic tests

While the contact stiffness likely determines the power equation of soil elastic stiffness, some other factors may also influence the elastic modulus. Houlsby and Schnaid [9] showed that the value of s increased as the density increased despite significant scatter in the loose sands testing data. Ahn-Dan and Koseki [10] showed that there was no apparent pattern in the magnitude of s in relation to variations in sample density. Makse et al. [11] pointed out the importance of the increasing number of contacts under pressure to explain the pressure dependence of elastic shear moduli. Unfortunately, the combined effect of the major factor (i.e., contact stiffness) and minor factor (i.e., density of the specimen) on soil elasticity has not yet been scrutinized.

To investigate the origin of the stress-level dependency of soil elasticity, we focused on the significance of microscopic parameters such as contact geometry, the evolution of the contact distribution, and changes in contact densities. We conducted a systematic investigation via the discrete element method to simulate small-strain, cyclic-loading tests. Two synthetic specimens, one loose and the other dense, were used for the simulations. The stress path experiment was simulated under various contact conditions, from which the patterns of stress-dependent elastic stiffness were analyzed.

2 Microscopic contact model

Let our hypothesis be that the power law of the contact model at the microscopic scale determines the power law of the elastic modulus at the macroscopic scale. To investigate this argument, it is necessary to employ a versatile model which is able to express various contact conditions. Thus we introduce a model proposed by Jäger [12] which assumes the geometry of the contact body to be an elastic sphere with local, axi-symmetric irregularity. Figure 1 illustrates contacting particles with small irregularities and the geometry of the contact surface with locally elastic half-space. The irregularity is expressed as $A_\alpha r^\alpha$ where r is the radius from the center of the rigid irregularity, A_α is the geometric constant, and α is the exponent determining the shape of the irregularity. In this study, three contact geometries are chosen: a conical irregularity ($\alpha = 1$), a spherical irregularity ($\alpha = 2$), and a flat surface ($\alpha = \infty$). Figure 2 shows the three different contact geometries.

The general expression of the contact normal force–displacement relationship is given by

$$k_n = df_n/d\delta_n \tag{2}$$

where k_n is the contact normal stiffness, f_n is the contact normal force, and δ_n is a contact normal displacement. In the case of the contact conditions shown in Fig. 1, the relationship between the contact force and displacement is defined as

$$f_n = c_n(\delta_n)^{1+1/\alpha}$$

$$\text{where } c_n = \frac{4G_g\alpha}{(1-\nu_g)(\alpha+1)}\left(\frac{\Gamma\left(\frac{\alpha+1}{2}\right)}{\sqrt{\pi}A_\alpha\Gamma\left(\frac{\alpha+2}{2}\right)}\right)^{1/\alpha} \tag{3}$$

where G_g and ν_g are the elastic shear modulus and Poisson's ratio of elastic particle grains respectively, and $\Gamma(x)$ is the gamma function. For example, the contact force–displacement relationship is $f_n = c_n(\delta_n)^2$ for the conical asperity ($\alpha = 1$), $f_n = c_n(\delta_n)^{3/2}$ for the spherical surface ($\alpha = 2$), and $f_n = c_n\delta_n$ for the flat contact surface ($\alpha = \infty$).

Differentiating and rearranging Eq. (3) with respect to f_n allows the tangent value of the contact normal stiffness k_n to be stated as

$$k_n = \frac{df_n}{d\delta_n} = \left(1 + \frac{1}{\alpha}\right)c_n^{\frac{\alpha}{1+\alpha}}(f_n)^{\frac{1}{1+\alpha}} \tag{4}$$

Consequently, the contact normal stiffness for the conical contact surface with $\alpha = 1$ can be expressed as

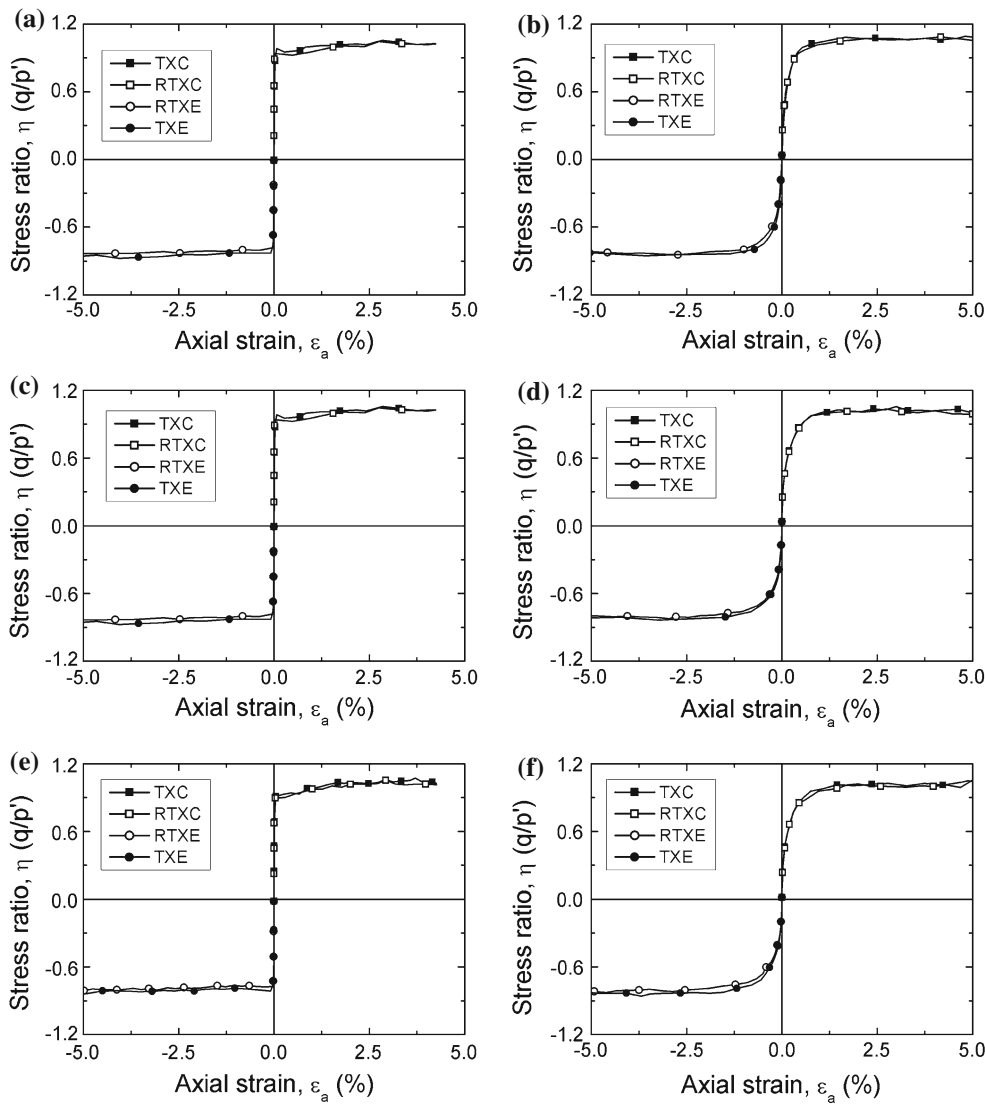$$k_n = \left(\frac{10G_g}{\pi(1-\nu_g)}\right)^{1/2}(f_n)^{1/2} \tag{5}$$

Fig. 6 Macroscopic stress ratio–axial strain relationships. **a** Conical contact in dense specimen, **b** conical contact in loose specimen, **c** spherical contact in dense specimen, **d** spherical contact in loose specimen, **e** flat contact in dense specimen, **f** flat contact in loose specimen

Table 4 Macroscopic friction angle at failure

Contact geometry	Density	TXC (°)	RTXC (°)	RTXE (°)	TXE (°)
Conical contact	Dense	26.8	26.7	29.2	29.2
$\alpha = 1$	Loose	27.2	27.1	29.4	30.6
Spherical contact	Dense	26.0	25.7	28.0	28.5
$\alpha = 2$	Loose	26.1	25.8	28.3	30.0
Flat contact	Dense	26.2	25.9	28.0	29.0
$\alpha = \infty$	Loose	26.5	25.9	27.3	28.6

Using Eq. (4), the contact normal stiffness for the spherical contact surface with $\alpha = 2$ becomes

$$k_n = \left(\frac{2G_g\sqrt{2R}}{3(1-\nu_g)} \right)^{2/3} (f_n)^{1/3} \tag{6}$$

Note that Eq. (6) is identical to the Hertzian contact model. The contact normal stiffness for the flat surface is independent of the contact force because $\alpha = \infty$ in Eq. (4), thus removing the term including f_n, so that

$$k_n = \frac{4G_g}{1-\nu_g} \tag{7}$$

Discrete element modeling (DEM) codes were modified to accommodate the three contact models described above. Regarding the tangential contact stiffness, we employed the expression proposed by Walton [13] which assumes that the tangential contact stiffness k_t has a linear relationship with k_n which can be stated as

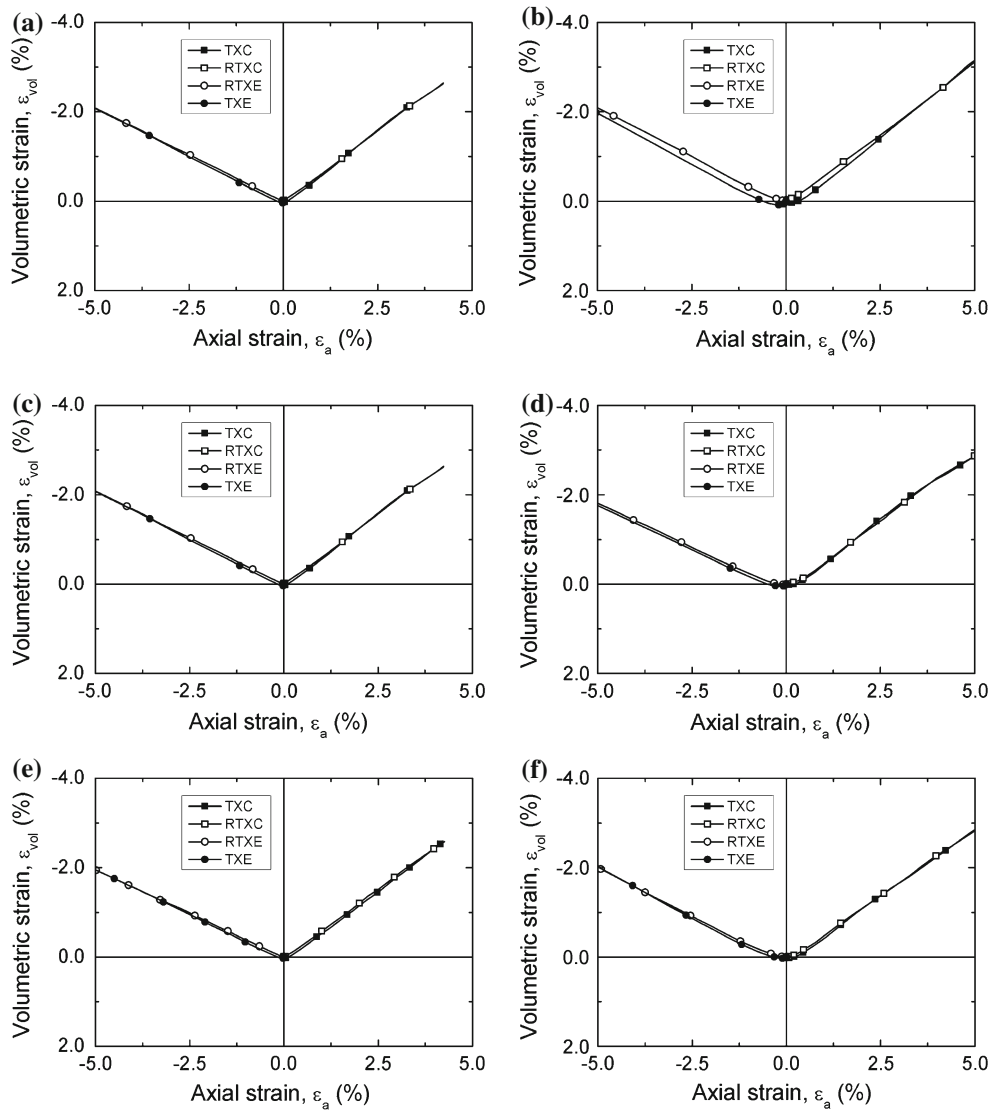$$k_t/k_n = 2(1-\nu_g)/(2-\nu_g) \tag{8}$$

Fig. 7 Macroscopic volumetric strain–axial strain relationships. **a** Conical contact in dense specimen, **b** conical contact in loose specimen, **c** spherical contact in dense specimen, **d** spherical contact in loose specimen, **e** flat contact in dense specimen, **f** flat contact in loose specimen

3 Discrete element simulations

Axi-symmetric stress loadings on an assembly of spherical particles were simulated using a non-commercial DEM code called OVAL developed by Kuhn [14,15]. The simulations performed in the present study involved a three-dimensional assembly of 10,000 uniform spheres with a particle diameter of 0.5 mm.

To prepare an initially isotropic granular assembly within a specified volume ($20 \times 20 \times 20$ mm), 10,000 seed particles with an artificially smaller diameter (0.1 mm) than the desired value were evenly distributed. Subsequently, the particles were numerically expanded until their diameters reached the desired value of 0.5 mm. The void ratio of the assembly at the completion of particle expansion was 0.56. This gener-

ation method involves multiple collisions between particles such that the particles push each other into an evenly-dense arrangement [16]. During expansion, the friction between the particles was purposely ignored for better stabilization. The external boundaries remained fixed during the expansion of the particles, and thus the particle configuration was locally adjusted to attain equilibrium. The model parameters for the simulation are summarized in Table 1.

The increment of time needed for stable computation is proportional to the square root of the particle mass divided by the sum of the stiffnesses acting on the particles. This suggests that the simulation of particles of high stiffness demands extremely small time increments and thus significant computational costs. To complete the simulations within a reasonable timeframe, the mass scaling technique [15,17],
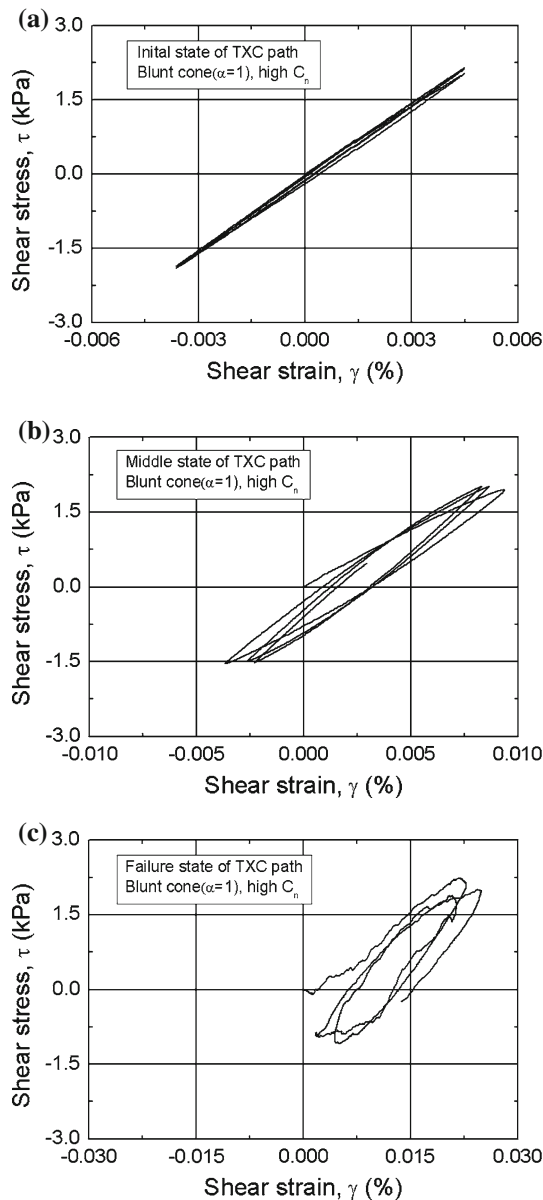
Fig. 8 Stress–strain curve obtained from the small strain cyclic shear tests for G_{hh}. **a** Linear response at $\eta = 0$, **b** non-linear response at $\eta = 0.5$, **c** unstable response at $\eta = 1.1$

which assumes a fictitious mass density for the particles, was employed to ensure stable and expedient simulations. Figure 3 shows the initial assembly of particles prior to stress path probing.

Both loose and dense specimens were prepared by adjusting the frictional coefficient between the particles. For the dense specimen, the particles began in a frictionless condition and a hydrostatic pressure of 10 kPa was applied to all the faces of the isotropic specimen. To obtain a loose specimen, friction was activated prior to applying the hydrostatic pressure such that the movement of the particles was more restrained than it was for the dense specimen. As mentioned

previously, three contact stiffness models were selectively employed so that a total of six specimens with different combinations of contact stiffness and density were prepared for the simulations. Table 2 summarizes the initial conditions of the six specimens. Note that small differences in the void ratio between the loose and dense specimens is common in discrete element methods [18].

Prior to stress probing, the specimen was loaded by increasing the hydrostatic pressure from 10 to 100 kPa, and this isotropic loading is called ISO. Four different stress paths—TXC, RTXC, RTXE, and TXE—were chosen for stress probing. Figure 4 shows the stress paths where the mean normal effective stress p' and deviator stress q are defined as

$$p' = (\sigma'_x + \sigma'_y + \sigma'_z)/3 \quad \text{and} \quad q = \sigma'_z - \sigma'_h \qquad (9)$$

where σ'_z is the vertical (axial) effective stress, σ'_x and σ'_y are the two horizontal stresses respectively, and σ'_h is the average value of the two horizontal stresses. Table 3 summarizes the notation used to describe the stress paths in Fig. 4. Note that instead of the minor principal stress, σ'_h was used to define the deviator stress and q to account for the minor differences in the two horizontal stresses from the simulations. The difference between the two horizontal stresses was consistently less than 1 kPa. From the same initial stress point, the axial stress increased along the TXC path, the radial stress decreased along the RTXC path, the axial stress decreased along the RTXE path, and the radial stress increased along the TXE path. The stresses were servo-controlled by moving the rigid boundary walls in accordance with continuous calculation of the wall stress defined as the average reaction force acting on the rigid wall divided by the area of the wall.

To measure the macroscopic elastic moduli along the stress path, a number of small-strain, cyclic-loading tests which are frequently performed in soil experiments [19] were simulated. We took advantage of the numerical simulation in that a specimen under a specific stress condition was "frozen" and later used for the small-strain, cyclic-loading tests. Every detail of information on the status of the assembly (e.g., the location of every particle and the contact force distribution) was stored at a specific stress point indicated by a small solid circle in Fig. 4. The stresses at which the cyclic loading tests were conducted were chosen at intervals of 10 kPa along the ISO path of increasing p' and at every increment of the stress ratio ($\eta = q/p'$) of 0.05 along the other stress-probing paths.

The small-strain, cyclic-loading test was conducted by tilting a pair of opposite rigid walls towards a given direction while holding the normal component of the wall stresses constant via a servo-control algorithm. Assuming that the "frozen" specimen preserved its cross-anisotropic nature likely induced from the initial depositional preparation, three tilting directions were chosen as shown in Fig. 5. The elastic shear modulus G_{hh} can be measured by slightly distorting
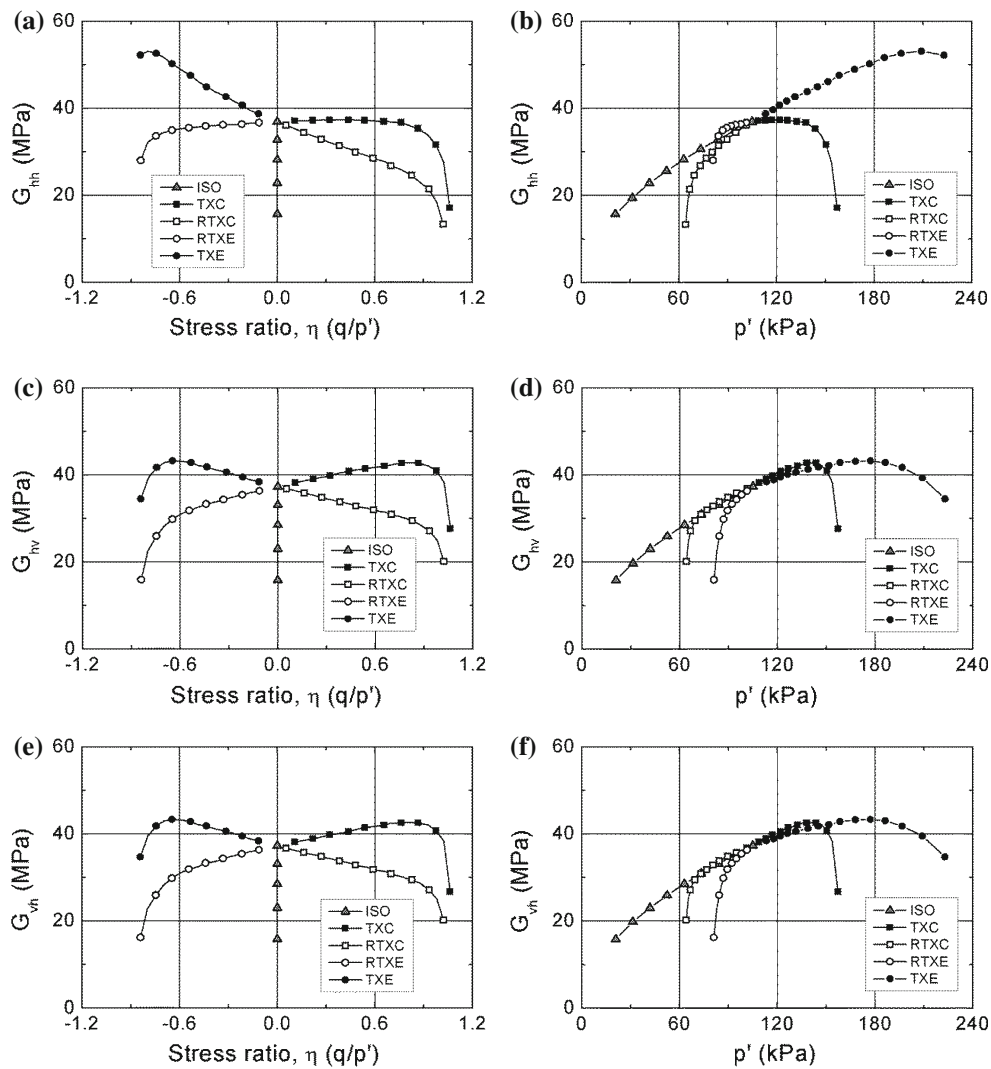
Fig. 9 Elastic shear moduli for conical contact in dense specimens. **a** η–G_{hh}, **b** p'–G_{hh}, **c** η–G_{hv}, **d** p'–G_{hv}, **e** η–G_{vh}, **f** p'–G_{vh}

the specimen in the horizontal plane as shown in Fig. 5a. As illustrated in Fig. 5b, c, the small-strain cyclic loadings in the vertical plane were used to measure the elastic moduli G_{vh} and G_{hv} respectively, which should be identical according to the theory of cross-anisotropic elasticity.

4 Results and discussion: macroscopic responses

Figure 6 shows the variation of the stress ratio during shearing. Stress–strain curves typical of frictional material were observed. One response to the axial compression was that the curves for TXC and RTXC overlapped; another was the axial extension of RTXE and TXE. The stress–strain curve for the dense specimens exhibits sharp stress peaks, while the curve for the loose specimens shows a mild change of slopes at the yield stress. The mobilized friction angles at the maximum

stress ratios in Fig. 6 are summarized in Table 4. The friction angles at the failure range from 26° to 31°, close to the inter-particle friction angle of 26.5° given by the frictional coefficient between particles. Particular variations caused by different contact geometries and densities were not observed.

Unlike the friction angle, the macroscopic stiffness represented by the initial slope of the stress–strain ratio curves is highly dependent on the initial density of the specimens. Figure 6 shows that the stress–strain curves of the dense specimens had a sharper slope than did the stress–strain curves of the loose specimens. As shown in Fig. 6, the stress–strain curves for the dense specimens consistently maintain linearity before a clear peak in stress, whereas the loose specimens show mild nonlinearity in the stress–strain curves before failure. Figure 7 shows that for both the loose and dense specimens, the volume expands similarly during shearing. This dilatancy might be expected if the void ratio values are
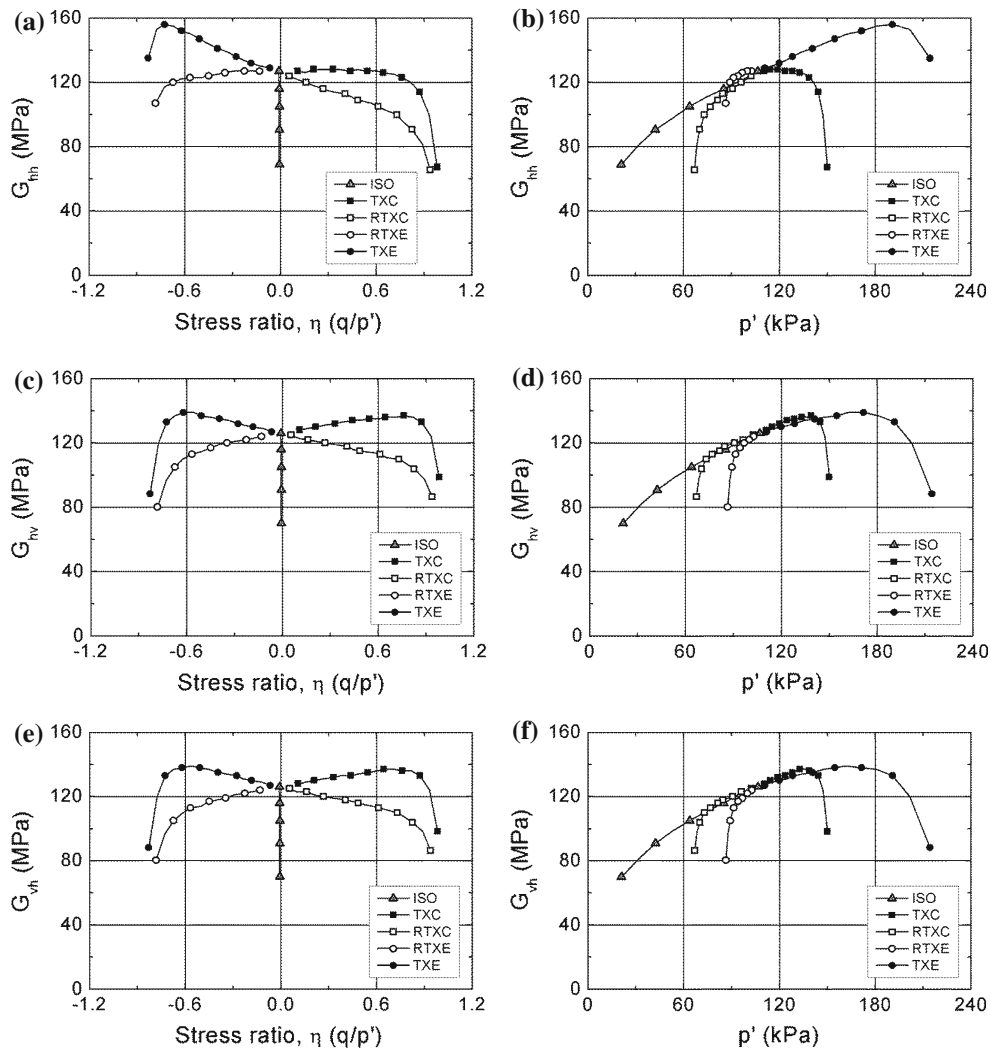
Fig. 10 Elastic shear moduli for spherical contact in dense specimens. **a** η –G_{hh}, **b** p'–G_{hh}, **c** η –G_{hv}, **d** p'–G_{hv}, **e** η –G_{vh}, **f** p'–G_{vh}

relatively low (e.g., 0.56–0.57) in both the dense and loose specimens, as summarized in Table 2.

Figure 8 shows three typical shear stress–strain curves obtained from the small cyclic loading tests on the dense specimen with a conical contact surface along the TXC path. An apparently linear and elastic stress–strain response was observed at the beginning of the shearing when $\eta = 0$ as shown in Fig. 8a. When = 0.5 in Fig. 8b, the stress–strain response exhibits nonlinear hysteresis, indicating energy dissipation due to friction. At $\eta = 1.1$ (close to the value at failure), the hysteretic stress–strain curve is not enclosed as shown in Fig. 8c. Except for a few cases near the point of failure, the initial linear portion of the stress–strain curve was used to define the elastic moduli G_{hh}, G_{vh} and G_{hv}.

Figures 9, 10 and 11 present variations among the three elastic shear moduli during stress probing on dense specimens. The effect of the packing density will be discussed after

providing data for the loosely packed specimens in Figs. 12, 13 and 14. The results show that G_{vh} is practically identical to G_{hv}, which confirms that the specimens preserve the cross-anisotropic nature induced by the deposition process during preparation. As described in Eq. (1), both G_{vh} and G_{hv} increase as p' increases. However, such increases do not continue as the stress ratio approaches a critical value corresponding to frictional failure. For example, the value of G_{hv} in the TXC path increased until $\eta = 0.9$ and then fell sharply as shown in Fig. 9. For the RTXC and RTXE paths in which the axial or radial stress decreased, the elastic shear moduli G_{vh} and G_{hv} decreased as predicted by Eq. (1) and subsequently fell sharply as η neared the failure values of 0.9 and −0.7 respectively. According to Eq. (1), it is expected that G_{hh} relates only to horizontal stress, as can be seen in Figs. 9, 10, 11, 12, 13 and 14. Along the TXC and RTXE paths in which the horizontal stress remained constant, the value
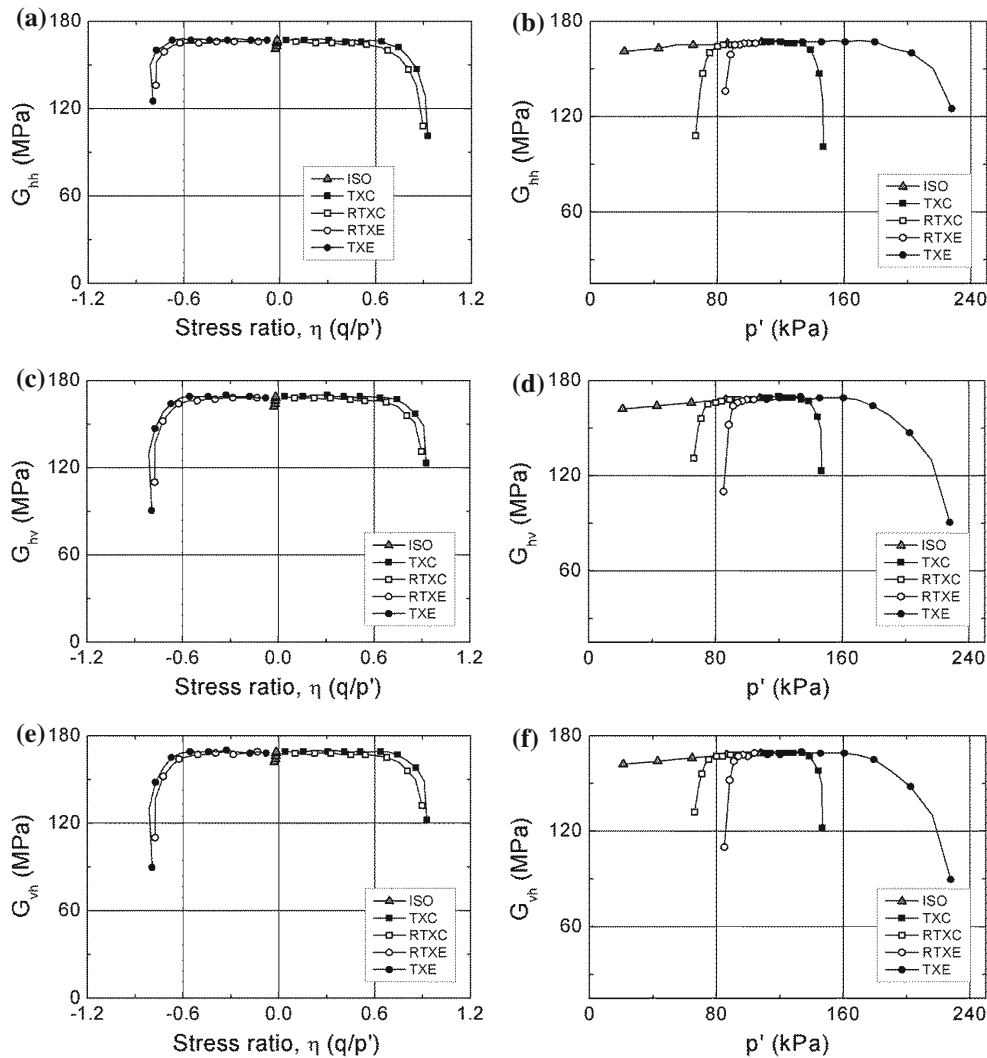
Fig. 11 Elastic shear moduli for flat contact in dense specimens. **a** η–G_{hh}, **b** p'–G_{hh}, **c** η–G_{hv}, **d** p'–G_{hv}, **e** η–G_{vh}, **f** p'–G_{vh}

of G_{hh} remained approximately constant until $\eta = \pm0.6$. A significant drop in the value of G_{hh} near the point of failure also appears as it does for G_{vh} and G_{hv}.

It should be noted that the elastic shear moduli for flat contact surfaces are insensitive to variations in stress. As shown in Fig. 11, all of the elastic moduli remained approximately constant until $\eta = \pm0.6$. This also means that the exponents in the empirical expression of Eq. (1) are zero in that the elastic shear modulus is independent of these stresses. The exponent used in Eq. (1) is closely related to the value of α used in the microscopic contact law in Eq. (4). For flat contact, the value of α is infinite, so the value of $1/(1+\alpha)$ in Eq. (4) becomes zero and is independent of the contact normal force as in Eq. (7). Consequently, the macroscopic responses reflect the microscopic behavior of the particle contacts.

Unfortunately, the relationship observed between the macroscopic response and microscopic cause in dense specimens does not seem to be valid in loose specimens. Figures 12, 13 and 14 show the simulation results for the

different elastic shear moduli of loose specimens. For the loose specimens with conical contact surfaces, G_{vh} and G_{hv} increase along the TXC and TXE paths, but not as quickly as they did with the dense specimens. In addition, a sharp reduction of the elastic moduli as η neared the failure value is not observed in the loose specimens. As shown in Fig. 14, it appears illogical to assume that the elastic moduli are independent of the variations in stress for specimens with flat contact surfaces.

The differences in the responses of dense and loose specimens can be investigated further by quantitatively evaluating the relationship between the elastic moduli and the stresses. Figure 15 summarizes the value of s, which is the sum of exponents m and n, by fitting the data shown in Figs. 9, 10, 11, 12, 13 and 14 into Eq. (1). The Levenberg–Marquardt iterative algorithm [20] was employed for nonlinear regression analysis to estimate the two exponents. The void ratio function in Eq. (1) is assumed to be $f(e) = (2.17 - e)^2/(1+e)$ as suggested by Hardin and Richart [21]. Note that
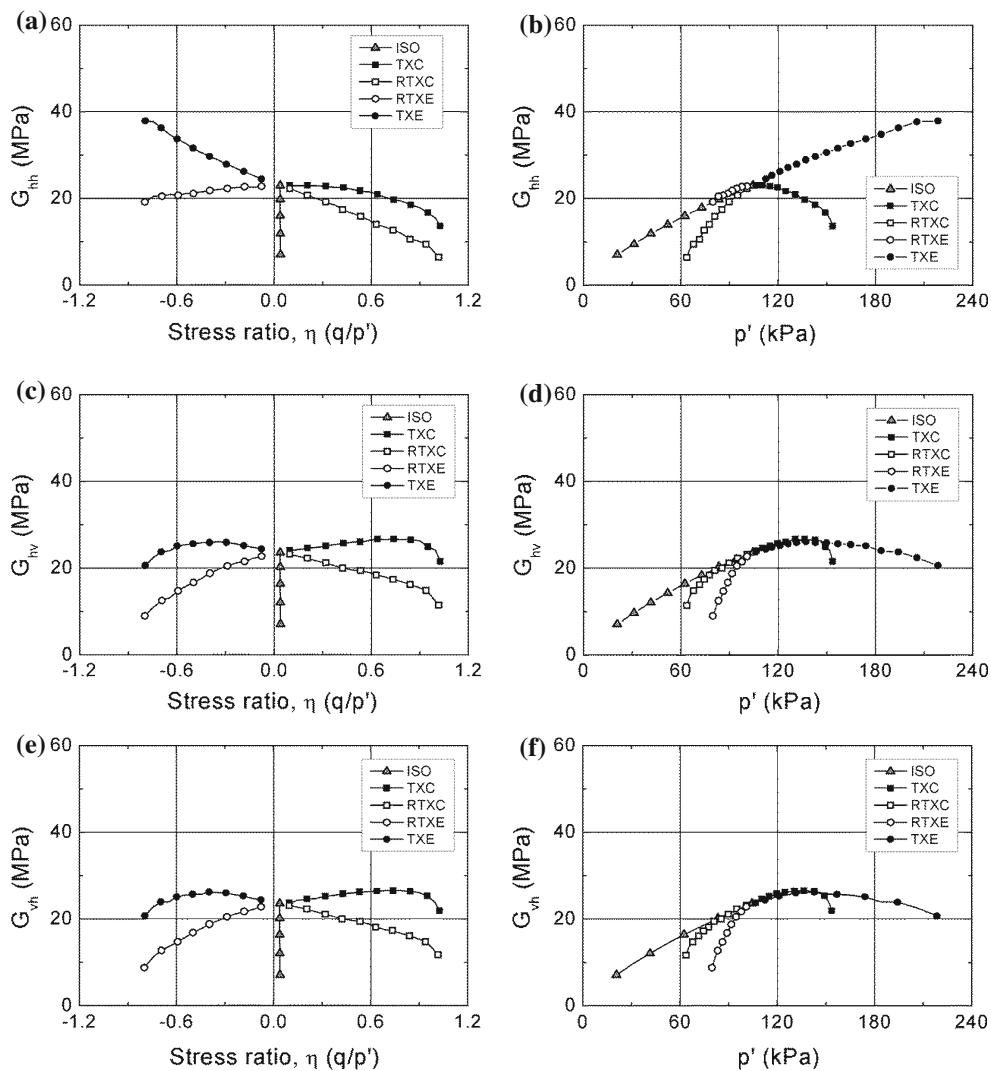
Fig. 12 Elastic shear moduli for conical contact in loose specimens. **a** η–G_{hh}, **b** p'–G_{hh}, **c** η–G_{hv}, **d** p'–G_{hv}, **e** η–G_{vh}, **f** p'–G_{vh}

interpolations of data were made for stress ratios ranging between −0.6 and +0.6 to exclude irrelevant data points corresponding to sharp drops in value when near failure. Note also that the reliability of the shear elastic moduli near failure, suggested in Figs. 9, 10, 11, 12, 13 and 14, is low due to severe nonlinearity in the stress–strain curves as illustrated in Fig. 8c. The parameters obtained from the regression analysis are summarized in Table 5.

As can be seen in Fig. 15, for a given contact surface condition, there is no difference among the values of *s* for the different elastic shear moduli. For the different contact surfaces, however, the values of *s* are quite different. As shown in Fig. 15, the dense specimens have values of $s = 0.5$ for conical contact surfaces, $s = 0.33$ for spherical surfaces, and $s = 0.0$ for flat surfaces. Surprisingly, these values are exactly the same as the exponents for the expressions of microscopic contact stiffness in Eqs. (5)–(7). These results

also confirm the conclusion reached by Jung and Chung [4] that the power function of normal contact stiffness manifests itself in the stress-level-dependent elastic moduli.

However, the values of *s* for the loose specimens (0.24–0.67) are much higher than they are for the dense specimens (0.02–0.51), with an average difference between the loose and dense specimens of approximately 0.2 for each contact surface condition. To explain the higher value of *s* in the loose specimens, we need to further investigate the differences in the microscopic responses of the loose and dense specimens.

5 Results and discussion: microscopic responses

The microscopic status of an assembly is statistically described by two quantities. The first is the coordination
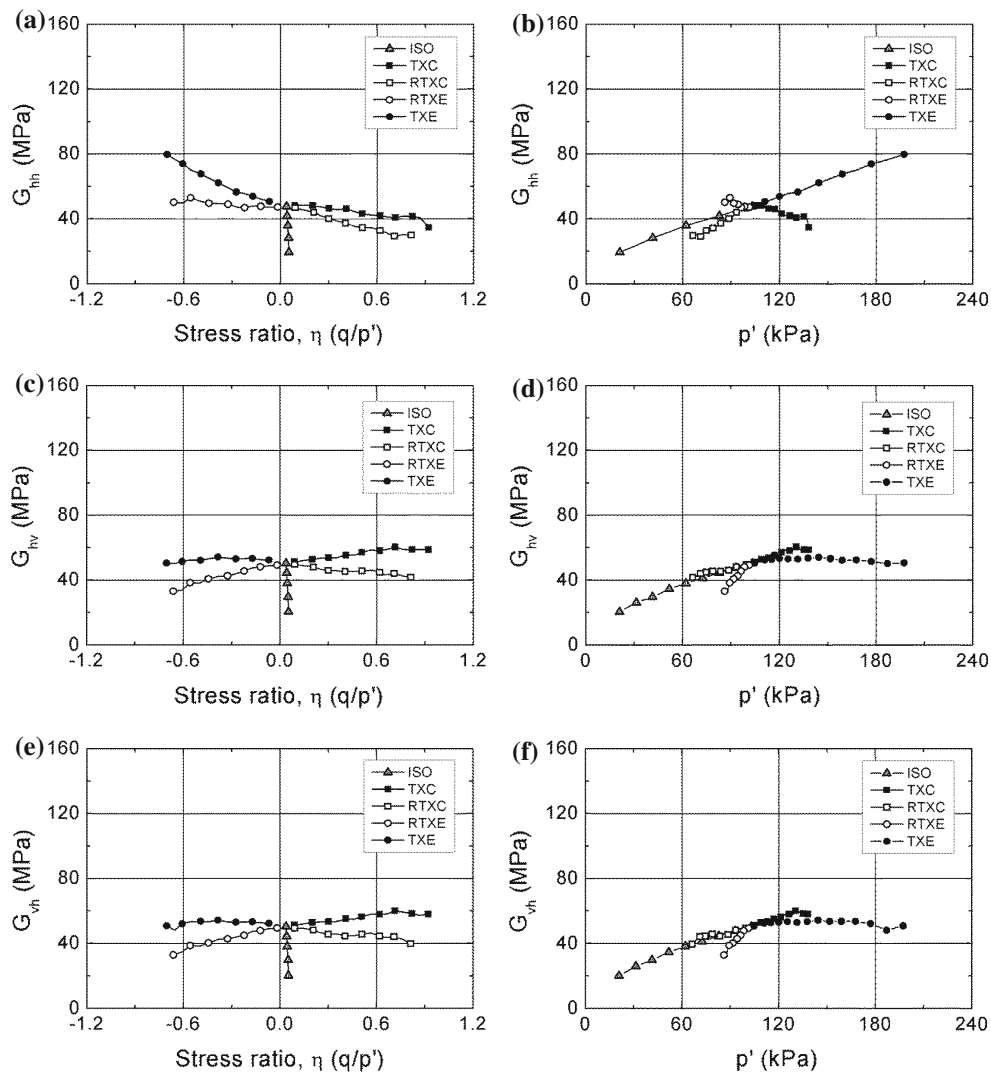
Fig. 13 Elastic shear moduli for spherical contact in loose specimens. **a** η–G_{hh}, **b** p'–G_{hh}, **c** η–G_{hv}, **d** p'–G_{hv}, **e** η–G_{vh}, **f** p'–G_{vh}

number C_n, which is the average number of contacts per particle and is a measure of the packing density. Table 2 summarizes the initial values of C_n for the different contact models. Second is the contact distribution function $E(\gamma, \beta)$, which measures the spatial distribution of contacts with respect to angular orientations γ and β in the spherical coordinate system. Figure 16 shows the spherical coordinate system used in this study. The contact distribution function for a symmetric assembly to the vertical axis [4,22,23] can be expressed as

$$E(\gamma, \beta) = \frac{3(1 + a \cos 2\gamma)}{4\pi(3 - a)} \tag{10}$$

which has a symmetry such that $E(\gamma + \pi) = E(\gamma)$ and is also independent of β. Using Eq. (10), a single parameter a, denoted as the degree of fabric anisotropy, can be used to describe the status of the contact normal distribution of the axi-symmetric assembly. The value of a can fall between

-1.0 and 1.0. The internal fabric structure becomes isotropic when $a = 0$. The majority of the contact normals are distributed vertically for positive a, whereas the contact normals are distributed horizontally for negative a. Figure 16b illustrates different probability distributions of the contact normal expressed by Eq. (10) with positive, negative and zero values for a. A detailed summary of the expressions of the contact distribution is given in Jang et al. [23].

Microscopic parameters C_n and a were evaluated using the data obtained from a "frozen" assembly, which was also used for the small-strain, cyclic-loading tests. Figures 17, 18 and 19 show the variations of C_n and a in loose and dense specimens with different contact models. For the dense specimens, the values of C_n and a remain constant within the range of stress ratios measuring between -0.6 and 0.6. Beyond this range of stress ratios, the value of C_n dramatically decreases, which is surprisingly similar to the macroscopic response—a
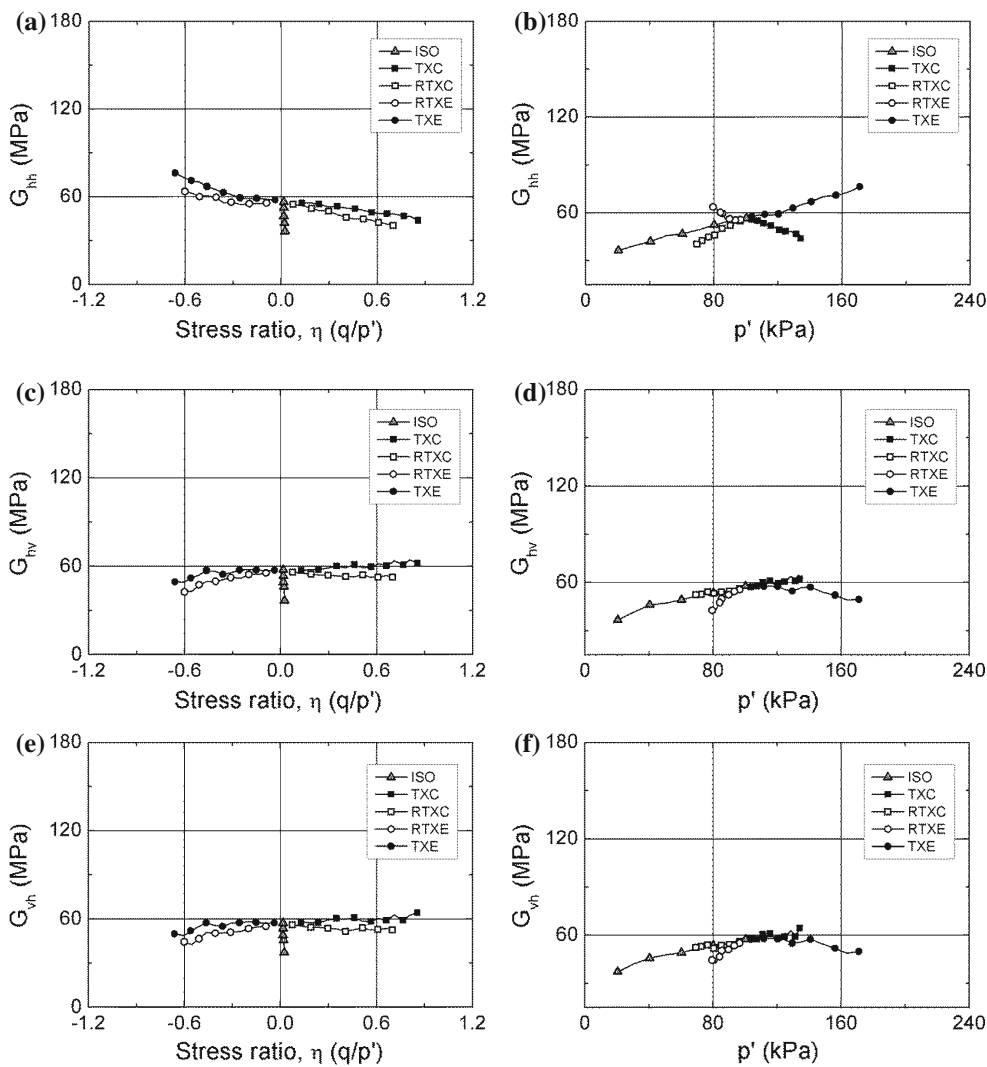
Fig. 14 Elastic shear moduli for flat contact in loose specimens. **a** η –G_{hh}, **b** p'–G_{hh}, **c** η –G_{hv}, **d** p'–G_{hv}, **e** η –G_{vh}, **f** p'–G_{vh}

sudden drop in the value of the elastic shear moduli in dense specimens. So long as the value of C_n remains constant, the value of a also remains constant at zero, implicating isotropy in the fabric structure. Beyond this range of constant value, the value of a significantly increases for stress ratios larger than 1.0 and decreases for stress ratios of less than −0.6.

The patterns observed in the loose specimens, however, are quite different from those observed in the dense specimens. For the conical contact model, the value of C_n varies nonlinearly—initially increasing and then decreasing—on the TXC and TXE paths, whereas the value of C_n gradually decreases without any constancy on the RTXC and RTXE paths. Unlike the dense specimens, the loose specimens do not exhibit a dramatic decrease of C_n near the failure values of the stress ratio. For the spherical and flat contact conditions, the value of C_n steadily increases. The variations of a in the loose specimens are also considerably different from

those in the dense specimens. Unlike the dense specimens, the loose specimens do not display a constant value of a for the stress ratios between −0.6 and 0.6. Instead the value of a nonlinearly varies with the stress ratio. This implies that the change of fabric structure manifested by the variation of a is much easier for the loose specimens than it is for the dense specimens. As shown in Table 2, a lower value of C_n for the loose specimens provides a higher degree of freedom in particle movement than for the dense specimens such that the contact points are continuously reallocated in favorable directions. In the dense specimens with high C_n values, the movement of particles is highly restrained but these restraints are eventually released at high stress ratios accompanying an abrupt reduction of in the value of C_n. Similar responses have also been observed by Maeda et al. [24].

The macroscopic response shows large values for s for the loose specimens, which implies that, with respect to
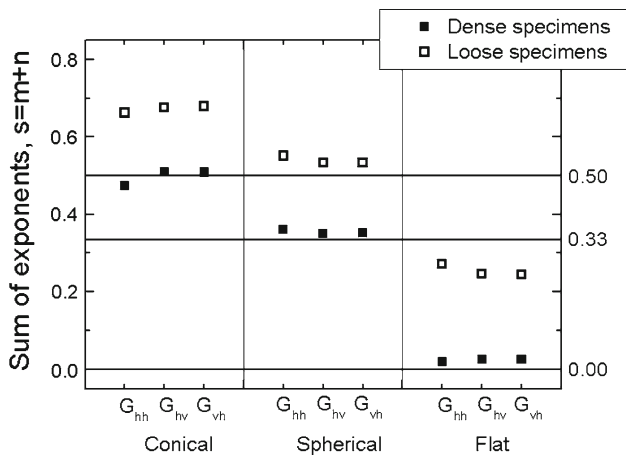
Fig. 15 Sum of exponent, s = m + n, for different contact geometries

Table 5 Parameters of empirical fitting equation with $f(e)$

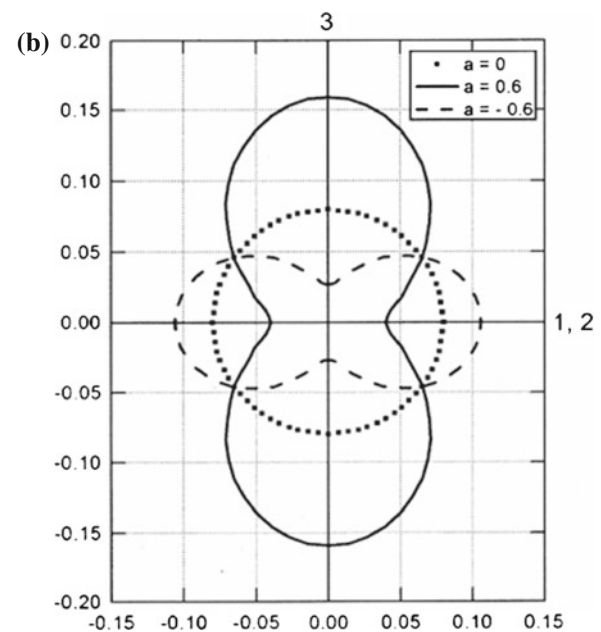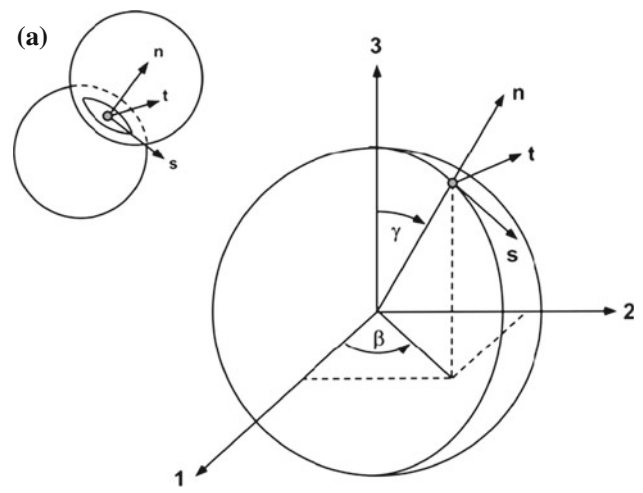| Model	Density	G	m	n	s = m + n	C
Conical contact surface	Dense	G_{hh}			0.475	21.03
		G_{hv}	0.273	0.237	0.510	21.45
		G_{vh}	0.234	0.275	0.509	21.43
	Loose	G_{hh}			0.662	12.99
		G_{hv}	0.322	0.353	0.677	13.31
		G_{vh}	0.354	0.325	0.679	13.32
Spherical contact surface	Dense	G_{hh}			0.361	71.95
		G_{hv}	0.189	0.160	0.349	73.74
		G_{vh}	0.162	0.190	0.352	73.75
	Loose	G_{hh}			0.551	29.92
		G_{hv}	0.176	0.357	0.533	29.59
		G_{vh}	0.345	0.189	0.534	29.56
Flat contact surface	Dense	G_{hh}			0.020	99.20
		G_{hv}	0.013	0.012	0.025	100.8
		G_{vh}	0.013	0.013	0.026	100.9
	Loose	G_{hh}			0.271	31.36
		G_{hv}	0.058	0.188	0.245	34.11
		G_{vh}	0.180	0.064	0.244	34.07

(a)

(b)

Fig. 16 Contact normal distribution function of axi-symmetric condition in spherical coordination system. **a** Spherical coordinate system, **b** contact normal distribution function

elastic shear moduli, the loose specimens are more dependent on stresses than the dense specimens are. The gap between the values for the loose and dense specimens supposes that the loose specimens have a causal agent other than contact stiffness, which has already been reflected in the low values for *s* for the dense specimens. It is estimated that microscopic variation in the particle contacts causes the additional dependency of the elastic shear modulus on the stresses in the loose specimens. Due to a lack of constraints corresponding to low C_n values, the loose specimens experience the continuous rearrangement of their particles as well as the transition of contact force chains during shearing.

This mobility in the contacts of the loose specimens eventually increases the dependency of the elastic shear moduli on stresses.

6 Conclusions

To investigate the origin of the stress-level dependency of soil elasticity, a series of stress-path experiments were conducted on loose and dense specimens with three different contact surface shapes (i.e., conical, spherical and flat). An analytical model assuming the geometry of the contact body as an elastic sphere with a local axi-symmetric irregularity was introduced in the discrete element simulations. To
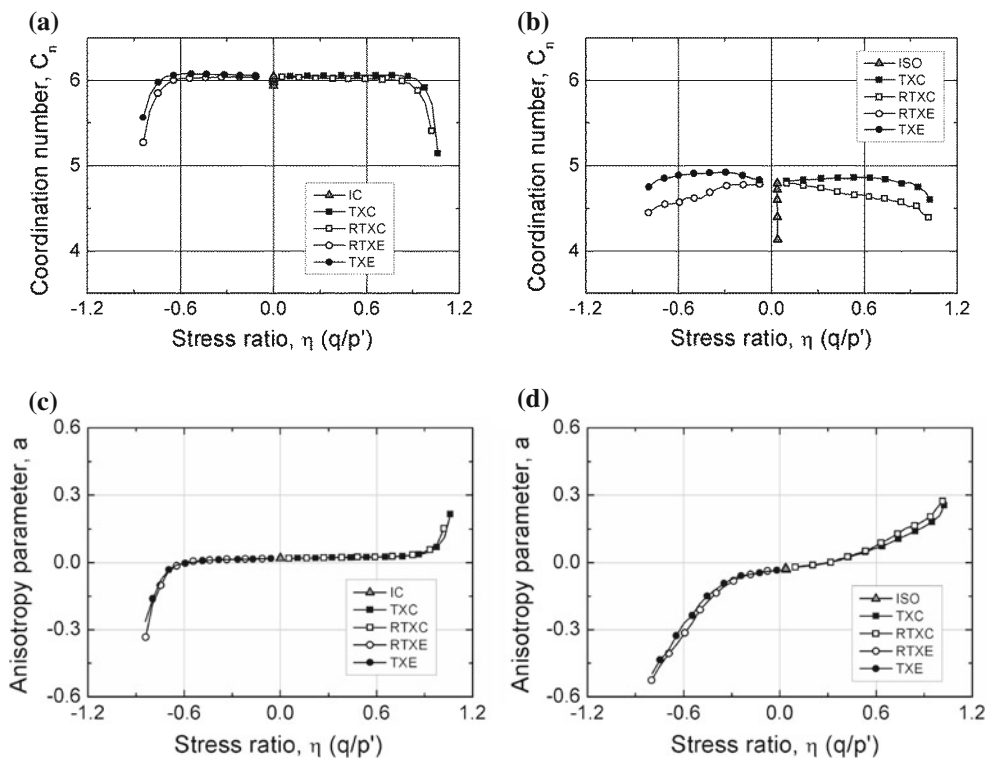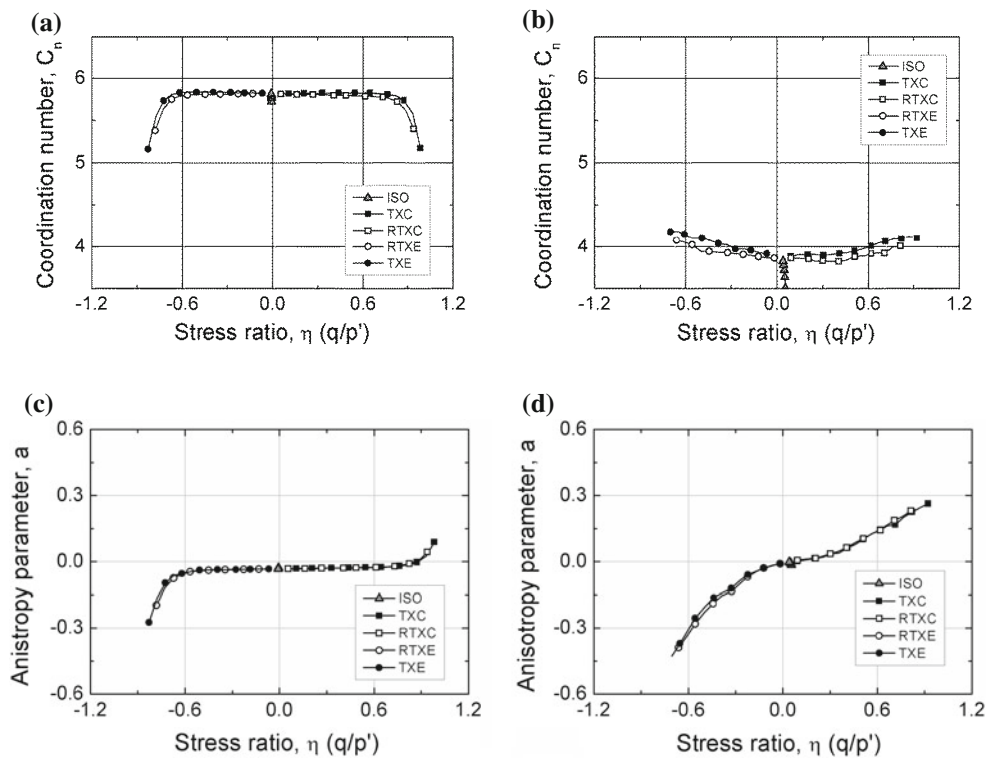
Fig. 17 Evolution of microscopic parameters for conical contact. **a** $\eta - C_n$ in dense specimens, **b** $\eta - C_n$ in loose specimens, **c** $\eta - a$ in dense specimens, **d** $\eta - a$ in loose specimens

Fig. 18 Evolution of microscopic parameters for spherical contact. **a** $\eta - C_n$ in dense specimens, **b** $\eta - C_n$ in loose specimens, **c** $\eta - a$ in dense specimens, **d** $\eta - a$ in loose specimens
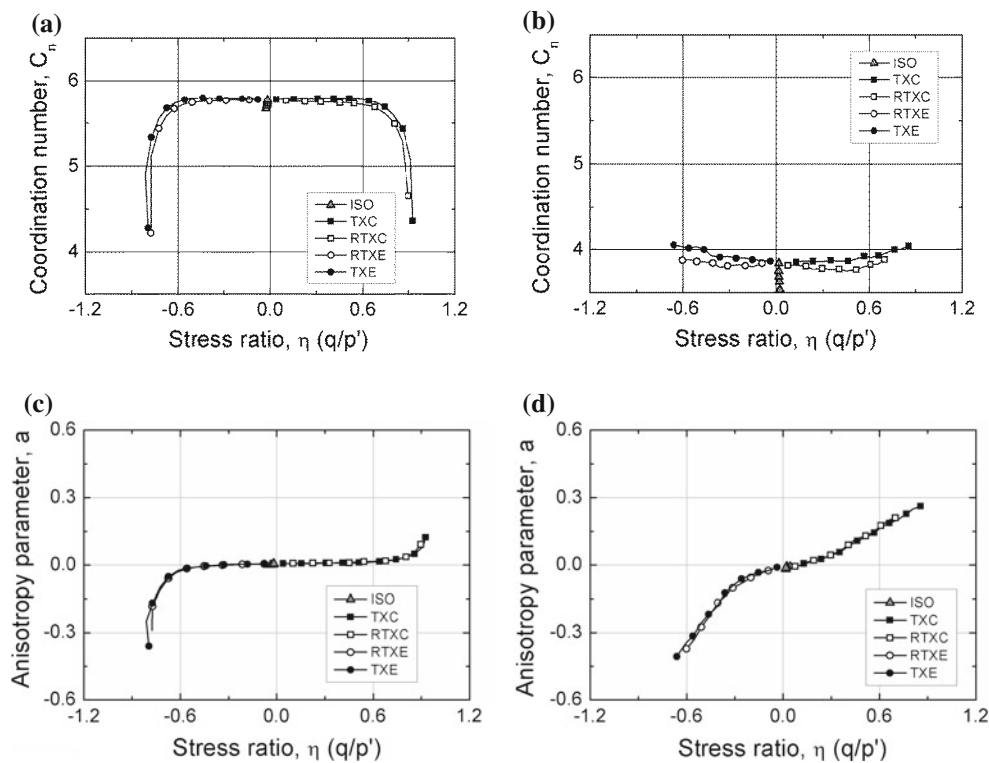
Fig. 19 Evolution of microscopic parameters for flat contact. **a** η –C_n in dense specimens, **b** η –C_n in loose specimens, **c** η –a in dense specimens, **d** η –a in loose specimens

evaluate the cross-anisotropic elastic shear moduli, small-strain, cyclic-loading tests were simulated on assemblies under the stress conditions along four stress probing paths. To study the stress-level dependency of soil elasticity, the sums of the exponents in the expression relating the elastic shear moduli and stresses has been focused upon.

For the dense specimens, the contact geometry had a decisive influence on the sum of the exponents, expressed as s. The simulation results show that $s = 0.5$ for the conical contact surface, 0.33 for the spherical surface, and 0.0 for the flat surface. Surprisingly, these values are exactly identical to the value of the exponents for the expressions of the contact stiffness equation. For the loose specimens, however, the value of s is much higher than it is for the dense specimens such that there is no correlation between the value of s and the exponent in the contact stiffness model.

Microscopic data explains the reason why the loose and dense specimens exhibit different degrees of stress-level dependency with regard to the elastic shear moduli. For the dense specimens with high C_n values, the internal structure represented by the degree of fabric anisotropy and the C_n value remain unchanged during shearing, thus leading to the coincidence of the s value and the exponent in the contact stiffness model. For the loose specimens with a low C_n value, however, the fabric structure evolves continuously during shearing, which results in an increase in the exponents in the

power function of the elastic modulus. The rearrangement of particles and the transition of contact force chains with the evolution of the fabric manifest themselves as increasing dependency with regard to the elastic moduli on the stresses in the loose specimens.

References

1. Hardin, B.O., Blandford, G.E.: Elasticity of particulate materials. J. Geotech. Eng. **115**(6), 788–805 (1989)
2. Duffy, J., Mindlin, R.D.: Stress–strain relations and vibrations of granular media. J. App. Mech. **24**(4), 585–593 (1957)
3. Cascante, G., Santamarina, J.C.: Interparticle contact behavior and wave propagation. J. Geotech. Eng. **122**(10), 831–839 (1996)
4. Jung, Y.H., Chung, C.K.: Role of micromechanics features on stress-level dependency of cross-anisotropic elastic moduli in granular soils. Comput. Geotech. **35**(2), 265–277 (2008). doi:10.1016/j.compgeo.2007.03.006
5. Bui, M.: Influence of some particle characteristics on the small strain response of granular materials. Ph.D. thesis, University of Southampton (2009)
6. Lee, C.-J., Huang, H.Y.: Wave velocities and their relation to fabric evolution during the shearing of sands. Soil Dyn. Earthq. Eng. **27**(1), 1–13 (2007)

7. Kohata, Y., Tatsuoka, F., Wang, L., Jiang, G.L., Hoque, E., Kodaka, T.: Modelling the non-linear deformation properties of stiff geomaterials. Geotechnique **47**(3), 563–580 (1997)
8. Clayton, C.R.I.: Stiffness at small strain: research and practice. Geotechnique **61**(1), 5–37 (2011)
9. Houlsby, G.T., Schnaid, F.: Interpretation of shear moduli from cone-pressuremeter tests in sand. Geotechnique **44**(1), 147–164 (1994)
10. AnhDan, L., Koseki, J.: Effects of large number of cyclic loading on deformation characteristics of dense granular materials. Soils Found. **44**(3), 115–123 (2004)
11. Makse, H.A., Gland, N., Johnson, D., Schwartz, L.: Why effective medium theory fails in granular materials. Phys. Rev. Lett. **83**(24), 5070–5073 (1999)
12. Jäger, J.: Uniaxial deformation of a random packing of particles. Arch. Appl. Mech. **69**(3), 181–203 (1999)
13. Walton, K.: Oblique compression of 2 elastic spheres. J. Mech. Phys. Solids **26**(3), 139–150 (1978)
14. Kuhn, M.R.: Heterogeneity and patterning in the quasi-static behavior of granular materials. Granul. Matter **4**(4), 155–166 (2003)
15. Kuhn, M.R.: OVAL and OVALPLOT: Programs for analyzing dense particle assemblies with the discrete element method (2006). http://faculty.up.edu/kuhn/oval/doc/oval_0618.pdf.
16. Bagi, K.: An algorithm to generate random dense arrangements for discrete element simulations of granular assemblies. Granul. Matter **7**, 31–43 (2005)
17. Zienkiewicz, O.C., Taylor, R.N.: The Finite Element Method. Volume 1: The Basis. Butterworth-Heinemann, London (2000)
18. Jiang, M.J., Konrad, J.M., Leroueil, S.: An efficient technique for generating homogeneous specimens for DEM studies. Comput. Geotech. **30**, 579–597 (2003)
19. Kuwano, R., Jardine, R.J.: On the applicability of cross-anisotropic elasticity to granular materials at very small strains. Geotechnique **52**(10), 727–749 (2002)
20. Levenberg, K.: A method for the solution of certain non-linear problems in least squares. Q. Appl. Math. **2**, 164–168 (1944)
21. Hardin, B.O., Richart, F.E.J.: Elastic wave velocities in granular soils. J. Soil Mech. Found. Eng. **89**(SM1), 33–65 (1963)
22. Chang, C.S., Sundaram, S.S., Misra, A.: Initial moduli of particulated mass with frictional contacts. Int. J. Numer. Anal. Meth. Geom. **13**(6), 629–644 (1989)
23. Jang, E.R., Jung, Y.H., Chung, C.K.: Stress ratio–fabric relationships of granular soils under axi-symmetric stress and plane-strain loading. Comput. Geotech. **37**(7–8), 913–929 (2010). doi:10.1016/j.compgeo.2010.07.010
24. Maeda, K., Sakai, H., Kondo, A., Yamaguchi, T., Fukuma, M., Nukudani, E.: Stress-chain based micromechanics of sand with grain shape effect. Granul. Matter **12**(5), 499–505 (2010). doi:10.1007/s10035-010-0208-5